ADVANCED PHOTONICS RESEARCH
Open Access
www.adpr-journal.com

Thin-Film Lithium Niobate Optical Modulators with an Extrapolated Bandwidth of 170 GHz

*Farzaneh Arab Juneghani, Milad Gholipour Vazimali, Jie Zhao, Xi Chen, Son Thai Le, Haoshuo Chen, Ehsan Ordouie, Nicolas K Fontaine, and Sasan Fathpour**

High-speed modulators with low driving voltage, low loss, and compact size are essential for future optical communication systems. Thin-film lithium niobate modulators have met each of these criteria separately, but simultaneous achievement of all of them has been challenging on this platform. Low driving voltage electro-optic modulators necessitate either a narrow gap between the electrodes or an elongated Mach–Zehnder arms, both of which adversely affect the microwave loss, hence the bandwidth. Herein, this trade-off is alleviated by placing the optical waveguides nonsymmetrically with respect to the electrodes and by including a dielectric buffer layer beneath the electrodes. Exploiting this novel design yields a modulator with a measured roll-off of only 2 dB from low frequencies up to 100 GHz, and with an extrapolated 3 dB bandwidth of 170 GHz. The measured voltage–length product of this subterahertz device is 3.3 V cm. Another device, optimized for a lower voltage–length product of 2.2 V cm, exhibits a 3 dB electro-optic bandwidth of 84 GHz. The devices are also tested for eight-level pulse-amplitude modulation (PAM-8) and demonstrate data rates of up to 240 Gb s^{-1} at 80 Gbaud, validating that the modulators are a propitious candidate for next-generation optical communication systems.

1. Introduction

To reduce the size, cost, and power consumption of current optical communication systems and to meet the requirements of future networks, it is crucial to develop modulators with high speed, low driving power, low loss, low cost, and small footprint.[1,2]

Currently, the majority of available commercial modulators are based on silicon (Si),[1,3–5] indium phosphide (InP),[6–8] and bulk lithium niobate (LN).[9] Despite impressive performance of modulators on these three platforms, none are capable of complying with the required criteria for the next generation of communication systems.

In recent years, modulators based on thin-film lithium niobate (TFLN) have emerged as a promising approach for ultrahigh bandwidth modulators with low driving voltages and small footprint.[10–19] The optical modes in TFLN waveguides are more compact than conventional LN counterparts, allowing the radio frequency (RF) electrode spacing to be reduced without causing detrimental optical absorption loss. Consequently, the overlap between the optical and electric fields increases, resulting in a lower driving voltage. Furthermore, using a substrate with a lower dielectric constant than bulk LN makes velocity mismatch between optical and electric fields easier, and thus improving bandwidth.[20] Another factor that can enhance the optical bandwidth is increasing the thickness of the SiO_2 insulating layer under the thin films in order to optimize the velocity mismatch.[12]

Despite the above inherent advantages of the TFLN platform, a delicate design is required to reach very high-performance modulators. For example, increasing the spacing between the electrodes can minimize the RF loss, a key parameter in determining the bandwidth, but at the expense of increasing the half-wave voltage, V_π.[21] Various TFLN modulators on silicon substrate have been reported to expand the 3 dB bandwidth of a single modulator up to 100 GHz and higher.[11,12,22,23] One method is to use a large gap between the electrodes, which leads to a bandwidth of more than 100 GHz, but with a $V_\pi > 13$ V,[11] due to the weak overlap between the electric and optical fields inside the gap. Another approach is to utilize asymmetric arms in a Mach–Zehnder modulator (MZM) and to operate at a null point of the transfer function. This approach, however, limits the operating wavelength and is sensitive to fabrication errors.[12]

The present work proposes a novel design to relieve the trade-off between bandwidth and V_π in order to achieve modulators with ultrahigh bandwidth and reasonably low voltage–length

F. Arab Juneghani, M. Gholipour Vazimali, E. Ordouie, S. Fathpour
CREOL, The College of Optics and Photonics
University of Central Florida
Orlando, FL 32816, USA
E-mail: fathpour@creol.ucf.edu

S. Fathpour
Department of Electrical and Computer Engineering
University of Central Florida
Orlando, FL 32816, USA

J. Zhao, X. Chen, S. T. Le, H. Chen, N. K. Fontaine
Nokia Bell Labs
600 Mountain Avenue, Murray Hill, NJ 07974, USA

The ORCID identification number(s) for the author(s) of this article can be found under https://doi.org/10.1002/adpr.202200216.

DOI: 10.1002/adpr.202200216

product ($V_\pi.L$). This is achieved by locating the optical waveguides in a nonsymmetric position with respect to the metal electrodes and by incorporating a thin dielectric buffer layer under the electrodes.

To validate these concepts, devices with and without nonsymmetric positioning and buffer layers are studied numerically and compared. Also, experimental results on two nonsymmetric modulators with different design parameters are presented. The first device has an extrapolated 3 dB electro-optic (EO) bandwidth of 170 GHz with a $V_\pi.L$ of 3.3 V cm. Another device exhibits a 3 dB bandwidth of 84 GHz with $V_\pi.L$ of 2.2 V cm. Moreover, eight-level pulse-amplitude modulation (PAM-8) up to 240 Gb s^{-1} is demonstrated using these modulators.

2. MZM with Noncentered Positioning of Optical Waveguides

High-speed MZMs in a push–pull configuration with traveling wave transmission lines on TFLN on Si substrate are studied in this work. Impedance matching, velocity matching, and minimal RF loss are three decisive factors in the design of high-speed modulators.[21] Impedance matching can be done by the proper design of the transmission lines. Velocity matching is significantly easier to achieve in TFLN devices compared to conventional LN devices, thanks to the low RF index of the insulating silicon dioxide layer, as well as the silicon or quartz substrates. Certain efforts have been made to minimize the RF loss by increasing the spacing between the electrodes at the cost of larger V_π,[11] or by designing segmented electrodes, which makes the velocity matching more challenging.[17,23]

Here, instead of positioning the optical waveguides at the center of the gap between the signal and ground electrodes, they are shifted closer to the signal electrode, whose vicinity has a stronger electric field profile. The parameter D (see **Figure 1**a) denotes the distance between the center of the optical waveguide and the center of the gap between the electrodes. Accordingly, the spacing between the electrodes can be kept large enough to minimize the RF loss and hence increase the bandwidth, while the electric and optical fields overlap heavily to reduce the V_π of the modulator. The only concern in such as arrangement is the increased optical propagation loss due to the proximity of metallic electrodes, which is mitigated by incorporating a thin silicon dioxide buffer layer beneath the electrodes. This buffer layer also reduces the RF effective index and helps with velocity matching.

In this work, the COMSOL Multiphysics software package is used to design and optimize the structure in Figure 1a to simultaneously achieve impedance matching, velocity matching, and low RF loss. Figure 1a depicts the cross-sectional view of these modulators. The device layer is a 500 nm-thick X-cut lithium niobate (LN) on an insulator layer on silicon substrate. The rib optical waveguides are 800 nm wide, which are formed through etching of the LN layer for 200 nm. Other design parameters of two different sets of modulators, later referred as modulator #1 and modulator #2, are provided in **Table 1**, whose performances are discussed in the next sections.

The effect of the nonsymmetric position of the optical waveguide and inclusion of a buffer layer on the 3 dB bandwidth and required length of MZMs are illustrated in **Figure 2**. The considered device is assumed to have fixed G and V_π, as well as a limit on optical propagation loss, with values given in the caption and rationalized later in this work. The two main parameters that determine the V_π of a modulator are the length of the transmission lines and the overlap integral between the optical and electrical fields. Moving the optical waveguide toward the signal electrode, i.e., increasing D, improves the overlap integral and hence the modulator can afford a shorter length for the same

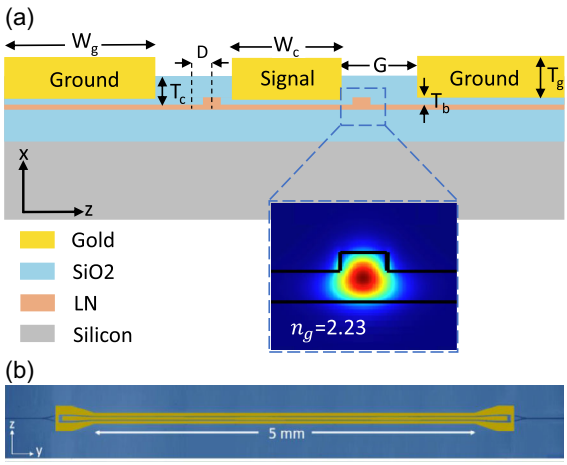

Figure 1. a) Cross-sectional view of the high-speed modulator with nonsymmetrical optical waveguides with respect to the electrodes to reduce the drive voltage, and the incorporated dielectric buffer layer to prevent absorption loss. The compact optical mode has a group index of 2.23. b) Microscopic image of a fabricated TFLN modulator.

Table 1. Dimension of modulators (μm).

MZM	G	D	W_c	W_g	T_g	T_b	T_c	Length
#1	5	0.6	12	40	1	0.2	0.8	5000
#2	10	2.6	22	40	1	0.2	0.8	5000

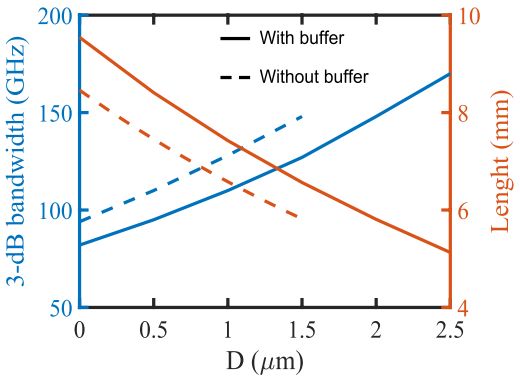

Figure 2. 3 dB bandwidth and length of modulator as a function of parameter D with and without a silicon dioxide buffer layer underneath the electrodes for fixed values of $G = 10\,\mu m$, $V_\pi = 6.6\,V$, and optical loss of <0.02 dB cm^{-1}. Bandwidth and length of modulator without the buffer layer are not presented for $D > 1.5\,\mu m$ because the resulting optical loss is more than 0.02 dB cm^{-1}.

V_π. On the other hand, the reduction in length results in a lower RF propagation loss and hence higher 3 dB bandwidth. Additionally, Figure 2 confirms that the embodied buffer layer reduces the overlap integral and degrades the performance of the device up to a certain value of D. However, it lessens the optical loss and thus allows the optical waveguide to be pushed closer to the signal electrode compared to the case without a buffer layer, which ultimately results in shorter devices with higher 3 dB bandwidths.

3. Results and Discussion

3.1. Static EO Measurement

The designed devices were fabricated by electron-beam lithography, dry etching, metalization, and deposition techniques on a TFLN die. More details on the fabrication steps can be found in the Supporting Information. A top-view microscopic image of a fabricated device is shown in Figure 1b. The end-butt coupling method is used to couple the light in and out of the modulators with polished waveguide facets. V_π is measured through a real-time modulation response by applying a 100 kHz triangular voltage sweep. **Figure 3**a,b shows the detected output signal by a photodetector versus the applied voltage for modulators #1 and #2 in Table 1, respectively. The respective V_π are 4.4 and 6.6 V, which corresponds to a voltage–length product ($V_\pi.L$) of 2.2 and 3.3 V cm, respectively. As expected, modulator #1 has a lower V_π owing to its smaller G. Modulators #1 and #2 have an extinction ratio of 23 and 20 dB, respectively. In addition, total insertion loss of these modulators under consideration is about 16 dB, which is mainly dominated by the facet loss.

Figure 3c investigates the effect of optical waveguide position on the value of V_π for modulator #2 with varying parameter D. In this plot, the V_π values are measured, while the optical losses are simulated using Ansys Lumerical. In the case of $D = 0$ µm—i.e., when the optical waveguides reside in the middle of the gap between signal and ground electrodes—$V_\pi = 12.6$ V. Increasing D—i.e., pushing the optical waveguides toward the signal electrode - results in reduced V_π at the cost of increasing optical propagation loss. However, for the case of $D = 2.6$ µm with V_π of 6.6 V, the optical loss is still kept below 0.02 dB cm^{-1} thanks to the incorporated buffer layer underneath the electrodes.

3.2. Electrical Characterization

Figure 4 compares the simulation and measured results for the characteristic impedance, effective index, and loss coefficient of modulator #2 in Table 1. The simulations and optimizations, illustrated in red, were done using COMSOL. The experimental values are extracted from the measured electrical S-parameters of the travelling-wave electrodes. These measurements were performed using a Vector Network Analyzer (VNA) and two ground-signal-ground (GSG) probes functioning up to 67 GHz, and were analyzed using a transmission-line circuit analysis.[24,25] A great agreement between the simulation and experimental results can be observed in Figure 4. Impedance matching is guaranteed because Z_m is in the range of 49–52 Ω over the RF spectrum. The RF effective index, n_m, is equal to 2.2, which is very close to the optical group index of 2.23 (see the inset of Figure 1a) and hence a great velocity matching is achieved for this modulator. The RF loss coefficient, α_m,

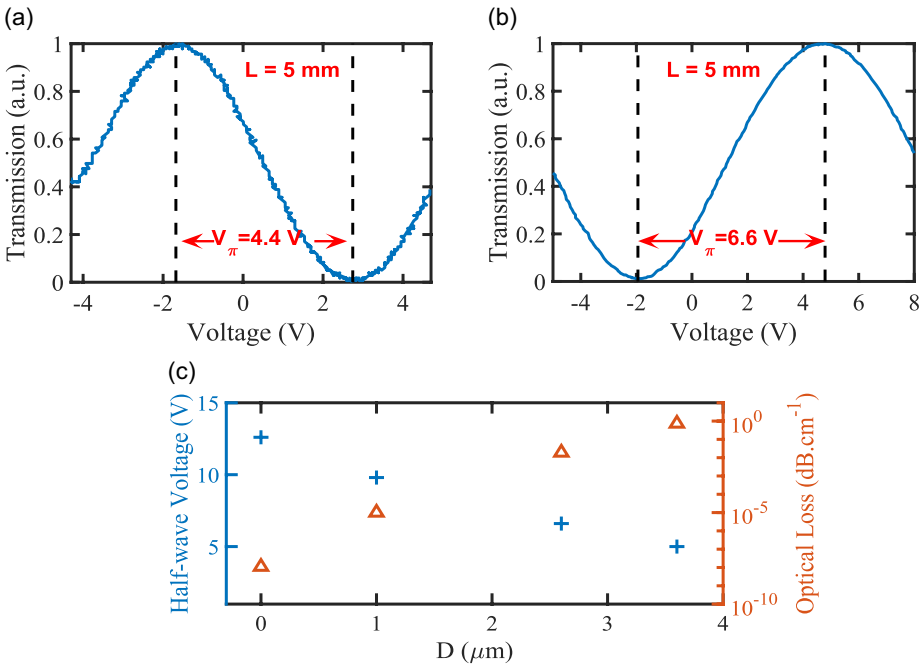

Figure 3. Normalized optical transmission of a) modulator #1 and b) modulator #2 as a function of the applied electrical voltage, showing V_π of 4.4 and 6.6 V, respectively, for 5 mm-long devices. c) Variation of V_π and optical loss versus the distance between the signal electrode edge and the center of the optical waveguide (parameter D).

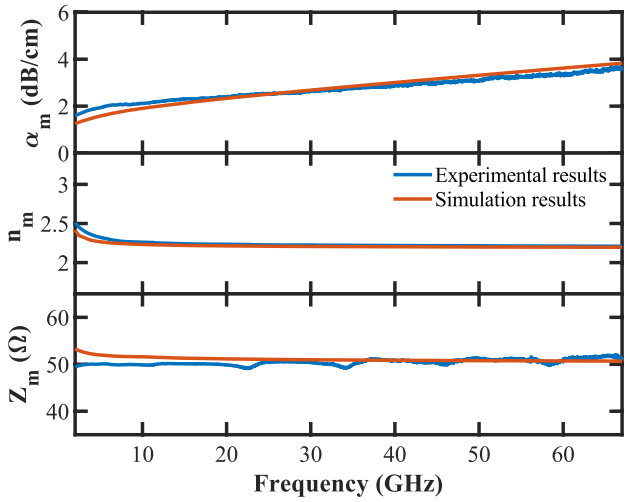

Figure 4. Simulation and experimental results of RF loss (α_m), RF effective index (n_m), and characteristic impedance (z_m) of the transmission line as a function of frequency for modulator #2.

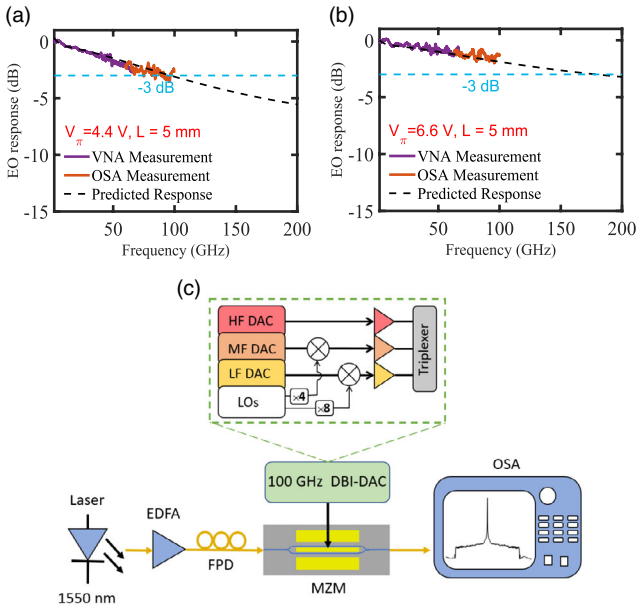

Figure 5. Measured EO responses referenced to devices with DC $V_\pi.L$ of a) 2.2 V cm and b) 3.3 V cm, showing ultrahigh 3 dB bandwidths of 84 GHz and well beyond 100 GHz, respectively. The EO responses—measured using a VNA up to 67 GHz and an Optical Spectrum Analyzer (OSA) from 60 to 100 GHz—are shown with solid violet and orange lines, respectively. c) Schematic of the experimental setup for measuring the OSA-based measurements. EDFA, erbium-doped fiber amplifier; FPC, fiber polarization controller; DBI-DAC, digital-band-interleaved digital-to-analog converter; HF, high frequency; MF: medium frequency; LF: low frequency.

which represents a combination of conductor and dielectric losses, has a reasonably low value of 3.6 dB cm^{-1} at 67 GHz or 0.44 dB cm^{-1} $GHz^{-1/2}$ due to the relatively large gap of $G = 10$ μm in this device.

3.3. EO Response

Figure 5a,b demonstrates the characterized EO bandwidth of modulators #1 and #2 in Table 1, respectively. To measure the EO response up to 100 GHz at an optical wavelength of 1550 nm, a two-step measurement was performed. The EO response for frequencies below 67 GHz is characterized using lightwave component analyzer (LCA), which includes a calibrated photodetector (PD) and a VNA. In order to apply the RF signal and to terminate the transmission line with a 50 Ω load, two high-speed GSG probes with 67 GHz bandwidth were used at the input and output sides, respectively. The experimental setup for ultrahigh-speed measurement up to 100 GHz is shown in Figure 5c. The details of this experimental setup are given in Supporting Information.

According to Figure 5a, the measured 3 dB EO bandwidth of modulator #1, which had $V_\pi.L$ of 2.2 V cm, is 84 GHz with only 3.6 dB roll-off from low frequencies to 100 GHz. Figure 5b illustrates that the measured 3 dB EO bandwidth of modulator #2 is well beyond 100 GHz with a roll-off of 2 dB from low frequency to 100 GHz. Using the extracted electrical characteristics and the analytical model described in ref. [26], the EO responses of the two modulators are extrapolated beyond the measurement limit of 100 GHz (see Section S1, Supporting Information, for details). The simulation results are added to Figure 5a,b. The simulation and experimental results perfectly match up to 100 GHz, thus gives us confidence that the simulations can be trusted to extrapolate the 3 dB modulation bandwidth of device #2. The corresponding 3 dB bandwidth of this modulator is 170 GHz, as evident in Figure 5b. Although comparable bandwidth has been reported in the past, the V_π in this device is quite high (13.4 V).[11]

This design extends the realm of optical modulators into the subterahertz range of RF frequencies with a low $V_\pi.L$ of 3.3 V cm, which confirms the effectiveness of the proposed and discussed nonsymmetric design. Because of the ultrahigh bandwidth of this modulator, it is possible to reduce V_π much further by increasing the modulator length while still having > 100 GHz bandwidth.

Figure 6 presents the RF V_π versus frequency for the two modulators, extracted from the measured EO response and DC V_π.[27] Modulator #2 with an ultrahigh bandwidth of 170 GHz has a $V_\pi.L$ of less than 4.1 V cm up to 100 GHz. This modulator with larger G has less variation in its EO response, as well as its RF V_π, over the frequency spectrum owing to its lower RF loss. Conductor loss and hence RF loss decrease in modulators with larger

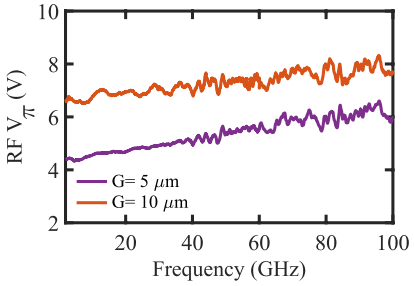

Figure 6. Extracted RF V_π from EO response shown in Figure 5a,b as a function of frequency.

gap due to the lower concentration of current along the electrodes' edges.[28,29] A summary of several ultrahigh-speed modulators on silicon and quartz substrates is provided in **Figure 7**, including the present modulators. Among modulators on the silicon substrate, our design shows the highest 3 dB bandwidth with a low $V_\pi.L$ that can operate in the full C-band due to symmetric Mach–Zehnder arm lengths in the MZM. Furthermore, using the measured electrode parameters from Figure 4, the 3 dB bandwidth of our presented approach has been predicted for longer lengths ($L = 0.75$, 1, 1.5, and 2 cm). It has been verified that employing segmented electrodes would help with a more uniform current concentration in the gap of a modulator.[17] The presented design can be easily augmented with segmented electrodes to further reduce the RF loss and consequently push the bandwidth to a greater extent.

3.4. Data Modulation

Figure 8a shows the employed setup for high-speed digital data modulation on modulator #1. The details of the experimental setup are given in Supporting Information.

In the first set of experiments for estimating the data modulation performance of the present devices, a 100 Gbaud on–off keying (OOK) signal was generated and transmitted. The received eye diagram is depicted in Figure 8b, showing a widely open eye. The bit-error rate (BER) of the captured signal at 100 Gb s^{-1} is 8.5×10^{-6}. Next, PAM-4 modulation is carried out at 106.25 and 200 Gb s^{-1}, resulting in a BER $< 1 \times 10^{-6}$ (error free) and 5.5×10^{-3}, respectively. Furthermore, this high-speed modulator enables transmitting higher data rates up to 240 Gb s^{-1} using PAM-8 modulation with a BER of 1.1×10^{-2}, which is within the tolerance of the typical 2% overhead soft-decision forward error correction (SD-FEC) limit of 2×10^{-2}. Overall, the results in Figure 8 indicate the excellent linearity of modulator #1 for high baud-rate optical transmissions. It should be noted that, due to the bandwidth limitation of the employed electronic digital-to-analog converter (DAC), the obtained performance is likely limited by the DAC and driver noise rather than the distortions of the optical modulator.

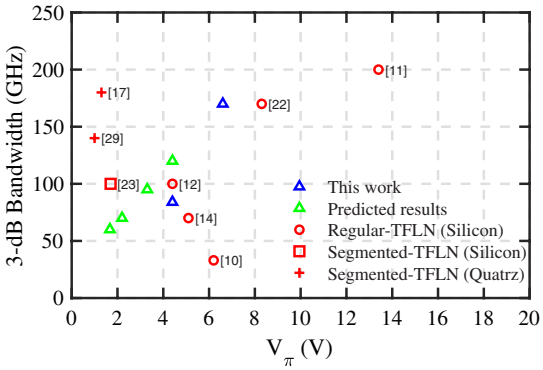

Figure 7. Performance comparison of the experimental results in this work (blue triangles), as well predicted results for devices with longer arms using the present approach (green triangles), with various prior works in the literature on quartz and silicon substrates, with and without segmented electrodes.

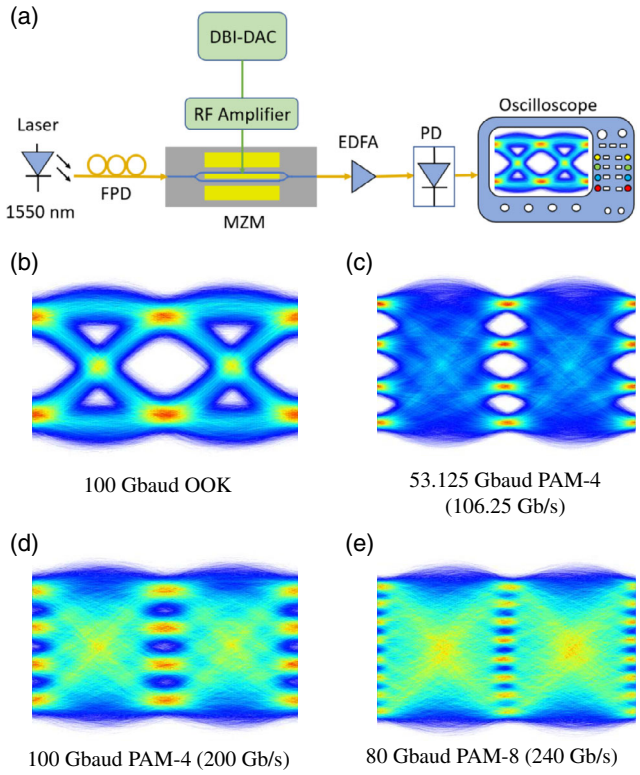

Figure 8. High-speed digital data modulation measurements. a) Schematic of the experimental setup for the data modulation using 67 GHz real-time oscilloscope. Eye diagrams for b) OOK modulation at data rates of 100 Gb s^{-1}. c,d) PAM-4 modulation at 53.125 Gbaud (106.25 Gb s^{-1}) and 100 Gbaud (200 Gb s^{-1}), respectively and e) ultrahigh speed PAM-8 modulation at 80 Gbaud (240 Gb s^{-1}).

The energy consumption per bit for data transmission within a traveling wave modulator is proportional to the root-mean-square voltage (V_{rms}) of the driving signal.[12] For PAM-4 modulation at data rate of 106.25 Gb s^{-1}, an electrical signal with V_{rms} of 656 mV is applied to the modulator. In this case, the energy consumption of the modulator is estimated to be 81 fJ bit^{-1}. To transmit high-speed PAM-8 modulation at data rate of 240 Gb s^{-1}, $V_{rms} = 1.23$ V, resulting in an energy consumption of 124 fJ bit^{-1}.

4. Conclusion

In conclusion, this work demonstrates that the trade-off between bandwidth and V_π of TFLN MZMs can be considerably alleviated by incorporating a buffer layer underneath the electrodes and by pushing the optical waveguides closer to the signal electrode to reduce V_π while preserving a reasonably large gap between the electrodes to achieve high bandwidth. The experimental results of two modulators with $V_\pi.L$ of 2.2 and 3.3 V cm, and with 3 dB EO bandwidth of 84 and 170 GHz, respectively, validate the superior performance of this novel type of modulators. These modulators could transmit 240 Gb s^{-1} of data using PAM-8 at 80 Gbaud with minor variation in RF V_π. Given the ease and robustness of fabrication, as well as the integrability with other

design concepts, such as segmented electrodes, this design can serve as a model for future optical networks, paving the way for TFLN EO modulators with low voltage and ultrahigh bandwidth in the subterahertz range and the various related digital and analog applications within this frequency range.

Supporting Information

Supporting Information is available from the Wiley Online Library or from the author.

Acknowledgements

M.G.V. and J.Z. contributed equally to this work. This work was partially supported by the National Science Foundation (NSF) Industry-University Cooperative Research Centers (IUCRC) program and L3Harris Technologies.

Conflict of Interest

The authors declare no conflict of interest.

Data Availability Statement

Research data are not shared.

Keywords

low voltage, thin-film lithium niobate modulators, ultrahigh-speed

Received: August 3, 2022
Revised: October 11, 2022
Published online:

[1] G. T. Reed, G. Mashanovich, F. Y. Gardes, D. Thomson, *Nat. Photonics* **2010**, *4*, 518.
[2] R. W. Tkach, *Bell Labs Tech. J.* **2010**, *14*, 3.
[3] Q. Xu, B. Schmidt, S. Pradhan, M. Lipson, *Nature* **2005**, *435*, 325.
[4] C. Sun, M. T. Wade, Y. Lee, J. S. Orcutt, L. Alloatti, M. S. Georgas, A. S. Waterman, J. M. Shainline, R. R. Avizienis, S. Lin, B. R. Moss, R. Kumar, F. Pavanello, A. H. Atabaki, H. M. Cook, A. J. Ou, J. C. Leu, Y.-H. Chen, K. Asanović, R. J. Ram, M. A. Popović, V. M. Stojanović, *Nature* **2015**, *528*, 534.
[5] A. Samani, E. El-Fiky, M. Osman, D. Patel, R. Li, M. Jacques, D. Plant, *Opt. Express* **2019**, *27*, 14447.
[6] M. Aoki, M. Suzuki, H. Sano, T. Kawano, T. Ido, T. Taniwatari, K. Uomi, A. Takai, *IEEE J. Quantum Electron.* **1993**, *29*, 2088.
[7] Y. Ogiso, J. Ozaki, Y. Ueda, N. Kashio, N. Kikuchi, E. Yamada, H. Tanobe, S. Kanazawa, H. Yamazaki, Y. Ohiso, T. Fujii, M. Kohtoku, *J. Lightwave Technol.* **2016**, *35*, 1450.
[8] Y. Ogiso, J. Ozaki, Y. Ueda, H. Wakita, M. Nagatani, H. Yamazaki, M. Nakamura, T. Kobayashi, S. Kanazawa, T. Fujii, Y. Hashizume, H. Tanobe, N. Nunoya, M. Ida, Y. Miyamoto, M. Ishikawa, in *Optical Fiber Communication Conf.*, Optical Society of America, **2019**, pp. M2F–2.
[9] E. L. Wooten, K. M. Kissa, A. Yi-Yan, E. J. Murphy, D. A. Lafaw, P. F. Hallemeier, D. Maack, D. V. Attanasio, D. J. Fritz, G. J. McBrien, D.E. Bossi, *IEEE J. Sel. Top. Quantum Electron.* **2000**, *6*, 69.
[10] A. Rao, A. Patil, P. Rabiei, A. Honardoost, R. DeSalvo, A. Paolella, S. Fathpour, *Opt. Lett.* **2016**, *41*, 5700.
[11] P. O. Weigel, J. Zhao, K. Fang, H. Al-Rubaye, D. Trotter, D. Hood, J. Mudrick, C. Dallo, A. T. Pomerene, A. L. Starbuck, C. T. DeRose, A. L. Lentine, G. Rebeiz, S. Mookherjea, *Opt. Express* **2018**, *26*, 23728.
[12] C. Wang, M. Zhang, X. Chen, M. Bertrand, A. Shams-Ansari, S. Chandrasekhar, P. Winzer, M. Lončar, *Nature* **2018**, *562*, 101.
[13] S. Sun, M. He, M. Xu, X. Zhang, Z. Ruan, L. Liu, X. Cai, in *2020 Optical Fiber Communications Conf. and Exhibition (OFC)*, IEEE, Piscataway, NJ **2020**, pp. 1–3.
[14] M. He, M. Xu, Y. Ren, J. Jian, Z. Ruan, Y. Xu, S. Gao, S. Sun, X. Wen, L. Zhou, L. Liu, C. Guo, H. Chen, S. Yu, L. Liu, X. Cai, *Nat. Photonics* **2019**, *13*, 359.
[15] A. Honardoost, K. Abdelsalam, S. Fathpour, *Laser Photonics Rev.* **2020**, *14*, 2000088.
[16] P. Rabiei, J. Ma, S. Khan, J. Chiles, S. Fathpour, *Opt. Express* **2013**, *21*, 25573.
[17] P. Kharel, C. Reimer, K. Luke, L. He, M. Zhang, *Optica* **2021**, *8*, 357.
[18] M. Xu, M. He, H. Zhang, J. Jian, Y. Pan, X. Liu, L. Chen, X. Meng, H. Chen, Z. Li, X. Xiao, S. Yu, S. Yu, X. Cai, *Nat. Commun.* **2020**, *11*, 1.
[19] X. Chen, G. Raybon, D. Che, J. Cho, K. Kim, in *2021 Optical Fiber Communications Conf. and Exhibition (OFC)*, IEEE, Piscataway, NJ **2021**, pp. 1–3.
[20] A. Rao, S. Fathpour, *IEEE J. Sel. Top. Quantum Electron.* **2017**, *24*, 1.
[21] A. Honardoost, F. A. Juneghani, R. Safian, S. Fathpour, *Opt. Express* **2019**, *27*, 6495.
[22] Y. Zhang, L. Shao, J. Yang, Z. Chen, K. Zhang, K.-M. Shum, D. Zhu, C. H. Chan, M. Lončar, C. Wang, *Photonics Res.* **2022**, *10*, 2380.
[23] Z. Wang, G. Chen, Z. Ruan, R. Gan, P. Huang, Z. Zheng, L. Lu, J. Li, C. Guo, K. Chen, L. Liu, *ACS Photonics* **2022**, *9*, 2668.
[24] D. M. Pozar, *Microwave Engineering*, John Wiley & Sons, Hoboken NJ **2011**.
[25] W. R. Eisenstadt, Y. Eo, *IEEE Trans. Compon. Hybrids Manuf. Technol.* **1992**, *15*, 483.
[26] J.-M. Liu, *Photonic Devices*, Cambridge University Press, Cambridge **2009**.
[27] D. D. Jones, Semiconductor devices for high-speed optoelectronics, by giovanni ghione: Scope: monograph and review. level: undergraduate, postgraduate and early career researcher, **2011**.
[28] D. F. Williams, S. Schwarz, In *1984 IEEE MTT-S Int. Microwave Symp. Digest.*, IEEE, Piscataway, NJ **1984**, pp. 453–454.
[29] M. Xu, Y. Zhu, F. Pittalà, J. Tang, M. He, W. C. Ng, J. Wang, Z. Ruan, X. Tang, M. Kuschnerov, L. Liu, S. Yu, B. Zheng, X. Cai, *Optica* **2022**, *9*, 61.